



# Formation Mechanism of AlN-MnS Complex Inclusions in Fe-5Mn-2Al-0.15C Medium Mn Steel

LI-BIN JIN,<sup>1</sup> SHU-GUO ZHENG,<sup>1,2</sup> and MIAO-YONG ZHU<sup>1</sup>

1.—School of Metallurgy, Northeastern University, 3-11, Wenhua Road, Shenyang 110819, China.  
2.—e-mail: zhengsg@smm.neu.edu.cn

The formation mechanism of AlN-MnS complex inclusions in Fe-5Mn-2Al-0.15C medium Mn steel was investigated under as-cast conditions by microstructure observation, thermodynamic analyses, and the Clyne–Kurz microsegregation model. The results showed the variations in the maximum and minimum partition coefficients for N and S were relatively large, and that the maximum diffusion coefficients of solute N, S, Mn and Al were more than 70% more than the minimum ones. Therefore, the variable partition coefficients and variable diffusion coefficients of solute elements under different temperatures should be considered in the Clyne–Kurz model during the solidification process. The partition coefficients of Al were higher than 1, segregating into the dendrite interior. However, the partition coefficients for elements N, Mn, and S were lower than 1, enriching in the residual liquid steel. By the Clyne–Kurz model considering the variable partition coefficients and variable diffusion coefficients, the precipitation temperatures of AlN and MnS were 1738 K and 1717 K during the solidification process, respectively. With experimental observation, the formation of AlN-MnS complex inclusions during the solidification process may be the AlN acting as a nucleation site for MnS, and then MnS wrapped or attached to the surface of AlN.

## INTRODUCTION

In recent years, with the increasing demand for improving passenger safety and reducing weight in automobile production, the automobile industry has been setting high standards for automotive steel. Medium Mn transformation-induced plasticity steels have attracted much attention because of their high strength, excellent ductility, and high energy absorption capacity.<sup>1,2</sup> Al-added medium Mn steels not only reduce weight but also greatly increase the stacking fault energy and effectively suppress delayed fracture induced by hydrogen embrittlement.<sup>3–7</sup> The Fe-Mn-C system is gradually being replaced by the Fe-Mn-Al-C system due to the many advantages of the addition of Al. At present, the cost of Fe-(4–6) Mn-(1–3) Al-(0.1–0.2) C medium Mn steel is relatively moderate and achieves a combination of strength and plasticity, showing

broad market prospects.<sup>8,9</sup> Also, the addition of microalloying elements (Nb, V, and Ti) to Fe-Mn-Al-C medium Mn steels, which can facilitate grain refinement through austenite, is a method to improve the plasticity.<sup>10–12</sup> The content of alloying elements Mn and Al in Fe-Mn-Al-C medium Mn steel is higher, so the segregation of these elements is more severe. Then, a large number of AlN-MnS complex inclusions precipitated during the solidification process, which seriously deteriorated the ductility and toughness of the steel.<sup>13–15</sup> Therefore, it is important to study the formation mechanism of AlN-MnS complex inclusions in Fe-Mn-Al-C medium Mn steels. The microsegregation of Al, N, Mn, and S increases the concentration product of AlN and MnS in the residual liquid phase, resulting in the formation of these inclusions during the solidification process. Accordingly, it is necessary to investigate the segregation behavior of Al, N, Mn, and S to understand the formation of AlN-MnS complex inclusions during the solidification process.

Many assumed and simplified microsegregation models have been developed to predict solute redistribution, such as the lever-rule model,<sup>16</sup> the Scheil model,<sup>17</sup> the Brody–Flemings model,<sup>18</sup> the Clyne–Kurz model,<sup>19</sup> the Ohnaka model,<sup>20</sup> and the Voller–Beckermann model.<sup>21</sup> The fundamental equations and assumptions of these microsegregation models are listed in Table I. In these models, several approximations have been made for the description of solute microsegregation. There were still some shortcomings in these models. During alloy solidification, the redistribution trend of the solute between the solid and liquid phases is determined by the solute partition coefficient. However, the partition coefficients of solute elements were assumed to be constant (see Table II) in most of the previous studies.<sup>22,23</sup> In fact, the partition coefficients of solute elements are easily influenced by the temperature and phase composition during the solidification process, usually as a variable value and not as a constant. The lever-rule model assumes that solute elements completely diffuse between the liquid phase and the solid phase, usually leading to the prediction not being valid because of the low diffusion rate in the solid phase. The Scheil model neglects diffusion of solute elements in the solid phase, which is not accurate for the solute concentration at the last stage of alloy solidification.<sup>24</sup> At present, research on the formation mechanism of AlN and MnS inclusions in Fe-Mn-Al-C steels has mainly focused on the idealized microsegregation model of the lever-rule and Scheil models. In fact, the finite nonzero diffusion of solute elements in the solid phase and the variable partition coefficients and variable diffusion coefficients under different temperatures should be taken into account during the solidification process. In most studies on the formation mechanism of AlN inclusions in Fe-Mn-Al-C steel, the partition coefficients of Al and N are

simplified to 0.6 and 0.27 during the solidification process, respectively, rather than a variable value. Shi et al.<sup>25</sup> investigated the formation of AlN inclusions in Fe-1.7Mn-1.05Al-0.07C steel by the Scheil model. They indicated that AlN can precipitate during the solidification process and the solid fraction ( $f_s$ ) was 0.841. However, the actual  $f_s$  of AlN was less than 0.841. Because the concentration product of AlN calculated by the Scheil model would be larger, the lever-rule model is more suitable for the element of N because the diffusion coefficient of N in the solid phase is larger. Therefore, some researchers have proposed that the concentration of N in the residual liquid phase is calculated by the lever-rule model. Liu et al.<sup>26</sup> reported the segregation of N and Al in high Mn twinning-induced plasticity (TWIP) steel ( $\sim 6\text{Al}\%$ ) calculated by the lever-rule and Scheil models, respectively and they found that AlN observed by means of high-temperature confocal scanning laser microscopy (HT-CSLM) were able to form in liquid steel. By the same calculation method, Alba and Nabeel et al.<sup>27–29</sup> analyzed the formation of AlN in high Al ( $\sim 6\text{Al}\%$ ) and medium Mn steel and obtained the critical content of N (5 ppm) for the formation of AlN form in liquid steel. Moreover, Liu et al.<sup>30</sup> investigated the finite nonzero diffusion of Mn and S in the solid

**Table II. Constant value of equilibrium partition coefficients in steel<sup>22,23</sup>**

Elements	$k^{\delta/L}$	$k^{\gamma/L}$
Al	0.6	0.6
N	0.25	0.48
Mn	0.77	0.785
S	0.05	0.035
C	0.19	0.34

**Table I. The fundamental equation and assumption of microsegregation models**

Models	Equations	Assumptions	Year	References
Lever-rule	$C_{L,i} = \frac{C_0}{1-(1-k_i)f_s}$	Complete diffusion of solutes in both liquid and solid phases	1922	16
Scheil	$C_{L,i} = \frac{C_0}{[1-f_s]^{(1-k_i)}}$	No diffusion in solid phase, complete diffusion in liquid	1942	17
B-F	$C_{L,i} = C_0[(1 - (1 - \beta_i k_i) f_s)^{\frac{(k_i-1)}{(1-\beta_i k_i)}}]$	Complete diffusion in liquid phase, finite nonzero diffusion in solid phase $\beta_i = 2 \alpha_i$	1966	18
C-K	$C_{L,i} = C_0[(1 - (1 - \beta_i k_i) f_s)^{\frac{(k_i-1)}{(1-\beta_i k_i)}}]$	Modified $\beta_i$ , ensure its physical reasonability	1981	19
Ohnaka	$C_{L,i} = C_0[(1 - (1 - \beta_i k_i) f_s)^{\frac{(k_i-1)}{(1-\beta_i k_i)}}]$	Modification of $\beta_i$ , useful for columnar dendrites	1986	20
V-B	$C_{L,i} = C_0[(1 - (1 - \beta_i k_i) f_s)^{\frac{(k_i-1)}{(1-\beta_i k_i)}}]$	Modified $\alpha_i = 2(\alpha_i + 0.1)$ , account for coarsening	1999	21

These microsegregation models present the redistribution of solute between the solid and liquid phases but without considering the variable partition coefficients and variable diffusion coefficients of solute elements under different temperatures during the solidification process.

phase by the Voller–Beckermann model in Fe-xMn-7Al-0.7C ( $x = 3, 10, 20, 30\%$ ) steels. With increasing Mn content, the  $f_s$  of MnS precipitation decreased, from 0.91 to 0.43. To date, studies on the formation mechanism of AlN-MnS complex inclusions in medium Mn ( $\sim 5\text{Mn}\%$ ) and high Al ( $\sim 2\text{Al}\%$ ) steel have rarely been reported. Therefore, in this study, the finite nonzero diffusion of solute elements in the solid phase and the variable partition coefficients and variable diffusion coefficients of elements were considered under different temperatures during the solidification process, which can accurately describe the precipitation of AlN-MnS complex inclusions in Fe-5Mn-2Al-0.15C medium Mn steel. Typical Fe-5Mn-2Al-0.15C medium Mn steel was prepared using a 50-kg vacuum-induction furnace. The formation mechanism of AlN-MnS complex inclusions under the as-cast conditions was analyzed by thermodynamic calculations and the Clyne–Kurz microsegregation model. The variable partition coefficients and variable diffusion coefficients of solute elements under different temperatures have been used in the Clyne–Kurz model during the solidification process. Furthermore, a scanning electron microscope (SEM; Carl Zeiss Ultra Plus) equipped with energy-dispersive spectroscopy (EDS) was employed for the morphology and chemical composition analyses to describe the precipitation behavior of AlN-MnS complex inclusions.

## EXPERIMENTAL PROCEDURES AND THERMODYNAMIC CALCULATIONS

### Materials Preparation

The Fe-5Mn-2Al-0.15C medium Mn steel was prepared in a 50-kg vacuum-induction furnace, and the chemical compositions of the steel are listed in Table III. Then, we investigated the formation of AlN and MnS inclusions in liquid steel and during solidification. The dimensions of the steel ingot and the positions of the specimens are shown in Fig. 1.

### Microstructure Characterization

The specimens used for microstructure observation were mechanically ground and polished. Subsequently, the morphology and chemical composition of the AlN-MnS complex inclusions in the specimens were characterized using SEM and EDS.

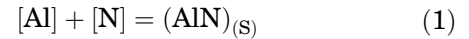
The polished specimens used for measuring the secondary dendrite arm spacing were etched in 5% saturated picric acid solution. The dendritic structure was observed using a digital microscope

(AxioCam MRc5), and the secondary dendrite arm spacing was statistically analyzed by the Image-Pro Plus 6.0 image analysis software.

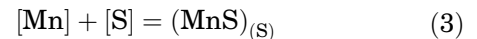
### Thermodynamic Calculations

#### Thermodynamic Equations of AlN and MnS Formation in Liquid Steel

The reaction equilibrium equations of AlN and MnS formation in liquid steel are described in Eqs. 2 and 4, and the solubility constants for AlN and MnS were described as:<sup>31,32</sup>



$$\begin{aligned} \log K_{\text{AlN}} &= \log \frac{a_{\text{AlN}}}{a_{\text{Al}} \cdot a_{\text{N}}} = \log a_{\text{AlN}} - \log a_{\text{Al}} - \log a_{\text{N}} \\ &= -\log(f_{\text{Al}}) \cdot [\% \text{Al}] - \log(f_{\text{N}}) \cdot [\% \text{N}] = \frac{-15850}{T} + 7.03 \end{aligned} \quad (2)$$



$$\begin{aligned} \log K_{\text{MnS}} &= \log \frac{a_{\text{MnS}}}{a_{\text{Mn}} \cdot a_{\text{S}}} = \log a_{\text{MnS}} - \log a_{\text{Mn}} - \log a_{\text{S}} \\ &= -\log(f_{\text{Mn}}) \cdot [\% \text{Mn}] - \log(f_{\text{S}}) \cdot [\% \text{S}] = \frac{-8817}{T} + 5.16 \end{aligned} \quad (4)$$

where  $a$  represents the activity and  $f_i$  is the Henrian activity coefficient of component  $i$  relative to the dilute solution. The value of  $f_i$  is calculated as:

$$\log f_i = \sum (e_i^j \cdot [pctj] + r_i^j \cdot [pctj]^2) \quad (5)$$

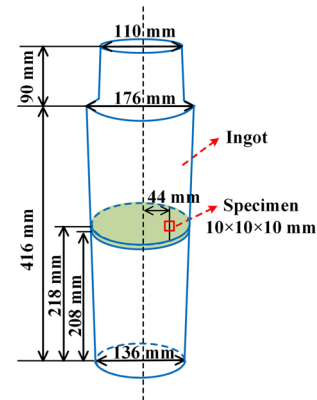


Fig. 1. The dimensions of the steel ingot and the positions of the specimen.

Table III. Chemical composition of the medium Mn steel, wt.%

C	Mn	Al	Si	Nb	V	S	N	P	O	Fe
0.17	4.96	1.93	0.23	0.07	0.04	0.0059	0.0025	0.0040	< 0.0005	Bal.

**Table IV. The first-order interaction parameters (1873 K)**

$e_i^j(j \rightarrow)$	C	Mn	Si	S	P	O	Al	N
Al	0.091	- 0.004	0.056	0.009	0.033	- 1.98	0.043	0.033
N	0.13 <sup>1</sup>	- 0.023	0.048	0.007	0.059	0.05	- 0.028	0.0166
Mn	- 0.07	0	- 0.0327	- 0.048	- 0.06	- 0.083	-	- 0.091
S	0.111	- 0.026	0.075	- 0.046	0.035	0.01	0.041	- 0.072

**Table V. The second-order interaction parameters (1873 K)**

$r_i^j(j \rightarrow)$	C	Mn	Si	S	P	Al
Al	- 0.004	-	- 0.0006	-	-	- 0.0011 + 0.17/T
N	-	0	0.0012	-	-	-
Mn	-	0	-	-	-	-
S	0.0058	0	0.0017	- 0.0009	0.0006	0.0009

( $i = \text{Al, N, Mn, S}; j = \text{Al, N, Mn, S, Si, Nb, V, P, O}$ ).

The first-order interaction parameters ( $e_i^j$ ) and the second-order interaction parameters ( $r_i^j$ ) used in this study are listed in Tables IV and V, respectively, and were taken from previous studies.<sup>26,32,33</sup>

Accordingly, the equilibrium solubility product  $K_{\text{AlN}}$  of AlN formation calculated by Eqs. 1, 2 and 5 is:

$$K_{\text{AlN}} = [\text{pct Al}][\text{pct N}] = 10^{7.089-15850/T} \quad (6)$$

In the case of MnS, the equilibrium solubility product  $K_{\text{MnS}}$  of MnS formation can be derived from Eqs. 3–5 as:

$$K_{\text{MnS}} = [\text{pct Mn}][\text{pct S}] = 10^{5.192-8817/T} \quad (7)$$

When the actual product of [% Al] and [% N] in the liquid phase exceeded the value of  $K_{\text{AlN}}$ , AlN inclusions formed in the liquid steel. Similarly, the precipitation of MnS from the liquid steel will occur if the actual concentration reaches the equilibrium solubility product ( $K_{\text{MnS}}$ ).

#### Microsegregation Models of AlN and MnS Formation During Solidification Process

The microsegregation of Al, N, Mn, and S will increase the concentration products of AlN and MnS in the residual liquid phase, resulting in these inclusions forming during the solidification process. Therefore, many assumed and simplified microsegregation models have been developed to predict solute microsegregation and redistribution.

The lever-rule model<sup>16</sup> assumes that solute elements diffuse completely between the liquid phase and the solid phase, and that the solidification of the alloy is an equilibrium process:

$$C_L = \frac{C_0}{1 - (1 - k_i)f_s} \quad (8)$$

The assumption of the lever-rule model leading to the prediction was not usually valid because of the low diffusion rate in the solid phase.

However, the Scheil model<sup>17</sup> neglects the diffusion of solute elements in the solid phase:

$$C_L = C_0[1 - f_s]^{(k_i-1)} \quad (9)$$

The solute concentration will become infinite when the solid fraction was equal to 1 at the last stage due to no diffusion of the solute element in the solid phase calculated by the Scheil model.

Considering the finite nonzero diffusion of solute elements in the solid phase, the microsegregation behavior of the solute can be described more accurately and realistically. The Brody–Flemings model,<sup>18</sup> which assumes incomplete back-diffusion of solute into the solid phase, can be defined as:

$$C_L = C_0[(1 - (1 - \beta_i k_i)f_s)^{\frac{k_i-1}{1-\beta_i k_i}}] \quad (10)$$

where  $\beta_i$  is the back-diffusion parameter, which is described as:

$$\beta_i = 2\alpha_i \quad (11)$$

where  $\alpha_i$  is the Fourier number of solute  $i$ , as:

$$\alpha_i = \frac{4D_s t_f}{\lambda_s^2} \quad (12)$$

where  $D^S$  ( $\text{m}^2 \text{s}^{-1}$ ) is the diffusion coefficient of the solute in the solid phase,  $\lambda_s$  is the secondary dendrite arm spacing, and  $t_f$  (s) is the local solidification time, defined as:

$$t_f = \frac{T_L - T_S}{C_R} \quad (13)$$

$\beta_i$  is a back-diffusion parameter, which is defined differently by researchers. The Clyne–Kurz model<sup>19</sup> modified  $\beta_i$  and ensured the physical reasonability, and  $\beta_i$  was defined as:

$$\beta_i = 2\alpha \left[ 1 - \exp\left(-\frac{1}{\alpha}\right) \right] - \frac{1}{2} \exp\left(-\frac{1}{2\alpha}\right) \quad (14)$$

Ohnaka<sup>20</sup> reported a quadratic solute profile in a solid, and Voller–Beckermann<sup>21</sup> considered the effect of coarsening on microsegregation by adding an additional term to the Fourier number, defined by:

$$\alpha_i^+ = 2(\alpha_i + \alpha^C), \alpha^C = 0.1 \quad (15)$$

Based on the above microsegregation models, the Clyne–Kurz model was more popular and widely applicable. Therefore, in this study, the AlN and MnS actual product concentrations during the solidification process were calculated by the Clyne–Kurz model and are:

$$Q_{\text{AlN}} = [\% \text{ Al}][\% \text{ N}] = [\% \text{ Al}]_0 \left[ (1 - (1 - \beta_{\text{Al}} k_{\text{Al}}) f_s)^{\frac{k_{\text{Al}} - 1}{1 - \beta_{\text{Al}} k_{\text{Al}}}} \right] [\% \text{ N}]_0 \left[ (1 - (1 - \beta_{\text{N}} k_{\text{N}}) f_s)^{\frac{k_{\text{N}} - 1}{1 - \beta_{\text{N}} k_{\text{N}}}} \right] \quad (16)$$

$$Q_{\text{MnS}} = [\% \text{ Mn}][\% \text{ S}] = [\% \text{ Mn}]_0 \left[ (1 - (1 - \beta_{\text{Mn}} k_{\text{Mn}}) f_s)^{\frac{k_{\text{Mn}} - 1}{1 - \beta_{\text{Mn}} k_{\text{Mn}}}} \right] [\% \text{ S}]_0 \left[ (1 - (1 - \beta_{\text{S}} k_{\text{S}}) f_s)^{\frac{k_{\text{S}} - 1}{1 - \beta_{\text{S}} k_{\text{S}}}} \right] \quad (17)$$

where  $[\% \text{ Al}]_0$ ,  $[\% \text{ N}]_0$ ,  $[\% \text{ Mn}]_0$  and  $[\% \text{ S}]_0$  are the initial contents of Al, N, Mn, and S in liquid steel, respectively,  $k_{\text{Al}}$ ,  $k_{\text{N}}$ ,  $k_{\text{Mn}}$ , and  $k_{\text{S}}$  are the equilibrium partition coefficients of Al, N, Mn, and S, respectively, and  $f_s$  is the solid fraction.

When the actual product of  $[\% \text{ Al}]$  and  $[\% \text{ N}]$  reached the value of  $K_{\text{AlN}}$  (calculated by Eq. 6), AlN inclusions were able to form during the solidification process. Similarly, the precipitation of MnS will occur if the actual concentration ( $Q_{\text{MnS}}$ ) exceeds the equilibrium concentration of  $K_{\text{MnS}}$  (calculated by Eq. 7).

In Eqs. 16 and 17, the relationship between the temperature of the liquid phase during solidification ( $T$ ) and the solid fraction ( $f_s$ ) is:

$$T = T_m - \frac{T_m - T_L}{1 - f_s \frac{(T_L - T_S)}{(T_m - T_S)}} \quad (18)$$

where  $T_m$ ,  $T_L$ , and  $T_S$  are the melting temperatures of pure Fe (1811 K, 1538 °C), the liquidus temperature, and the solidus temperature, respectively.

In addition, the equilibrium solubility products of AlN and MnS (Eqs. 6 and 7) can also be expressed by Eq. 18.

## RESULTS AND DISCUSSION

### Thermodynamic Analysis of AlN and MnS Formation in Liquid Steel

The calculated stability diagram of AlN and MnS formation in liquid steel is shown in Fig. 2. The dashed and solid lines represent the solubility products of AlN and MnS inclusions at liquidus ( $T_L = 1778$  K) and solidus temperatures ( $T_S = 1709$  K), respectively, which were calculated by ThermoCalc software. In current steel compositions, the contents of Al, N, Mn, and S are low, and the composition positions are in the solid phase far from the liquid region. It is clear that AlN and MnS were unable to form in the liquid steel due to the initial content of Al and N, Mn and S being lower than those at the liquidus temperature, respectively. According to the solubility product of AlN and MnS inclusions at liquid temperature, the critical contents of N and S for AlN and MnS formation in liquid steel are 0.0075 and 0.3546 wt.%, respectively.

### Thermodynamic Analysis of AlN and MnS Formation During Solidification Process

As shown in Fig. 2, the equilibrium concentration products of Al and N and Mn and S cannot reach the liquid steel, so the AlN and MnS inclusions cannot precipitate in the liquid steel. However, when the temperature of the steels dropped below the liquidus temperature, the microsegregation of Al, N, Mn, and S increased the concentration product of AlN and MnS in the residual liquid phase, resulting in the formation of AlN and MnS inclusions during the solidification process.

According to the Clyne–Kurz microsegregation model, it can be expressed as a function of the segregation of elements  $i$ . These parameters include the secondary dendrite arm spacing ( $\lambda_S$ ), the cooling rate ( $C_R$ ) of the steel ingot, the equilibrium partition coefficient ( $k_i$ ), and the diffusion coefficient ( $D^S$ ) of these elements. It is known that the value of  $\lambda_S$  can be used to predict the cooling rate of the ingot, and investigators<sup>16</sup> have shown that, for this study ( $[\text{C}] > 0.15$  wt.%), the relationship is:

$$\lambda_S = 143.9 \cdot C_R^{-0.3616} \cdot C_C^{(0.5501 - 1.996C_C)} \quad (19)$$

where  $\lambda_S$  is the secondary dendrite arm spacing ( $\mu\text{m}$ ),  $C_C$  is the carbon content (wt.%), and  $C_R$  is the cooling rate ( $\text{K s}^{-1}$ ).

Figure 3 shows the dendrite structure in the medium Mn steel, and the measured average  $\lambda_S$  is  $71 \pm 13 \mu\text{m}$  based on many measurements; hence, the estimated cooling rate (by Eq. 19) for the steel ingot during solidification is approximately 2.5 K/s.

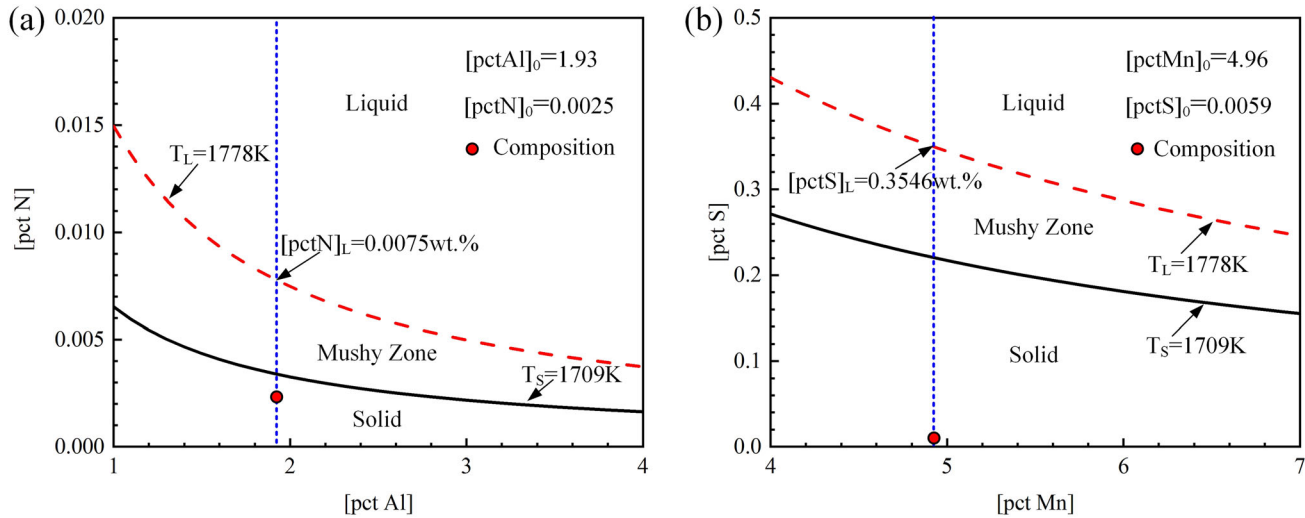


Fig. 2. The stability diagram of AlN and MnS formation in liquid steel: (a) AlN; (b) MnS.

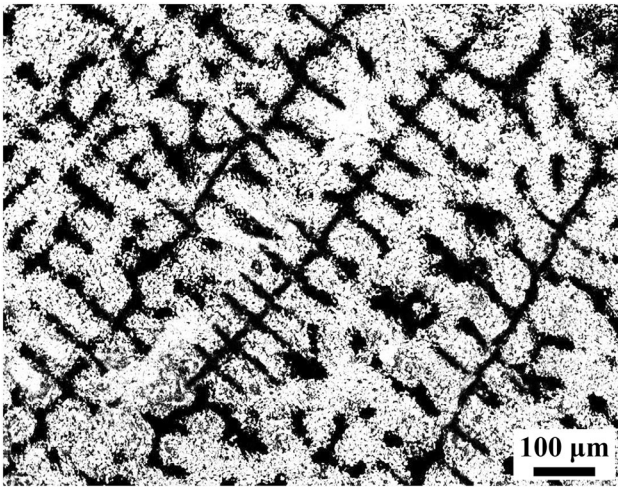


Fig. 3. The typical dendrite structure of the medium Mn steel.

The phase composition fractions and solidification sequence in medium Mn steel are shown in Fig. 4. During the cooling of the steel, the  $\delta$  phase is predicted to first form from the liquid phase at 1778 K, and then a peritectic reaction occurs at 1715 K, leading to a temperature range where the mixed liquid, the  $\delta$  phase, and the  $\gamma$  (austenite) phase exist simultaneously with the liquid phase disappearing at 1709 K. Finally, the phase of medium Mn steel is fully transformed to the  $\gamma$  phase at 1594 K.

To require the equilibrium partition coefficients of Al, N, Mn, and S ( $k^{\delta/L}$  and  $k^{\gamma/L}$ ), the concentrations of Al, N, Mn, and S in the liquid, and the  $\delta$  and  $\gamma$  phases were calculated by Thermo-Calc software, as shown in Fig. 5. During the solidification process, the content of Al in the  $L + \delta$  phase first decreased, and then gradually increased in the  $L + \delta + \gamma$  phase, while the content of the solute elements N, Mn, and S increased in different phases.

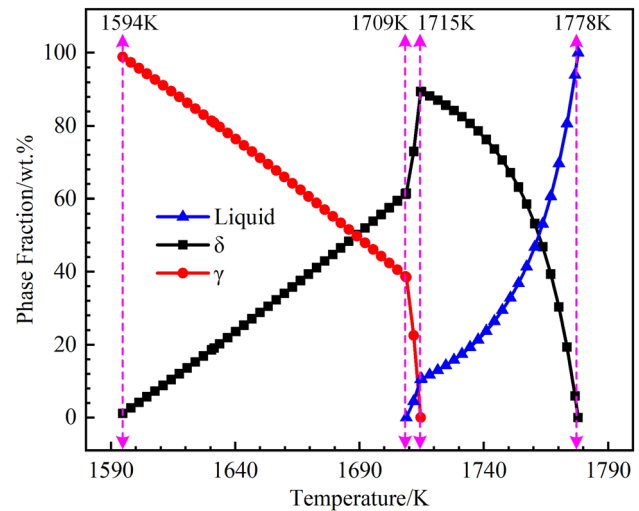


Fig. 4. The phase composition fractions and solidification sequence in medium Mn steel during cooling.

The equilibrium partition coefficients of Al, N, Mn, and S in the  $\delta$  and  $\gamma$  phases ( $k^{\delta/L}$  and  $k^{\gamma/L}$ ) are shown in Fig. 6a and b. The partition coefficients of Al were higher than 1, which showed negative segregation. Therefore, it will segregate into internal dendrites, consumed in the residual liquid steel during the solidification process. The segregation behavior of Al was consistent with the studies of Zhang et al.<sup>34</sup> in high-Al ( $\sim 2$  Al %) TWIP ( $\sim 23$  Mn %) steel and Lu et al.<sup>35</sup> in high-nitrogen ( $\sim 0.4$  N %) (0.006–0.076 Al %) stainless bearing steel. The equilibrium partition coefficients for elements N, Mn, and S were lower than 1, which presented positive segregation; therefore, they preferred to segregate into the interdendritic area, enriching the residual liquid steel. Meanwhile, the values of  $k^{\gamma/L}$  were closer to 1 than those of  $k^{\delta/L}$ , illustrating that the segregation degree of Al, N, and Mn between the  $\gamma$  and liquid phases was lower than that between the

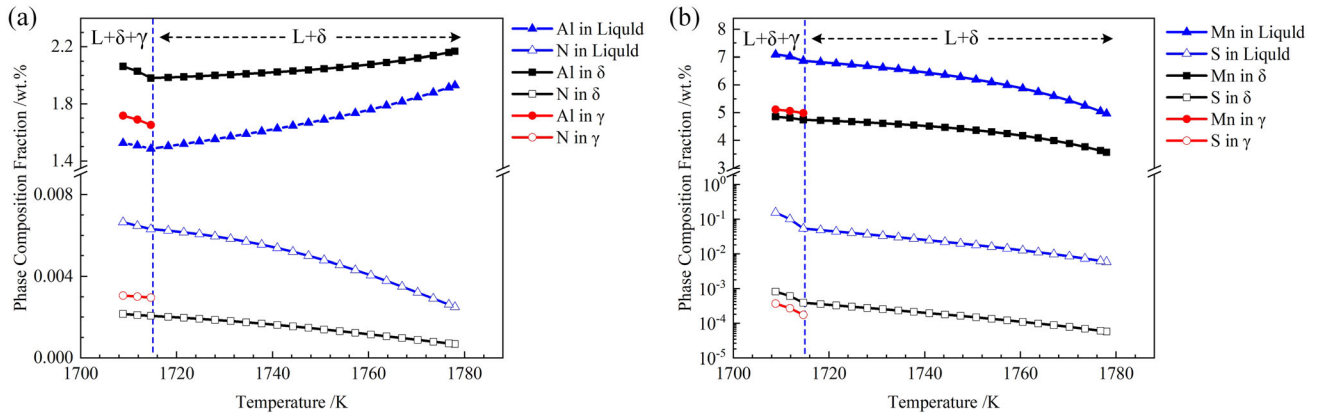


Fig. 5. The phase composition fractions in medium Mn steel during solidification process: (a) Al and N; (b) Mn and S.

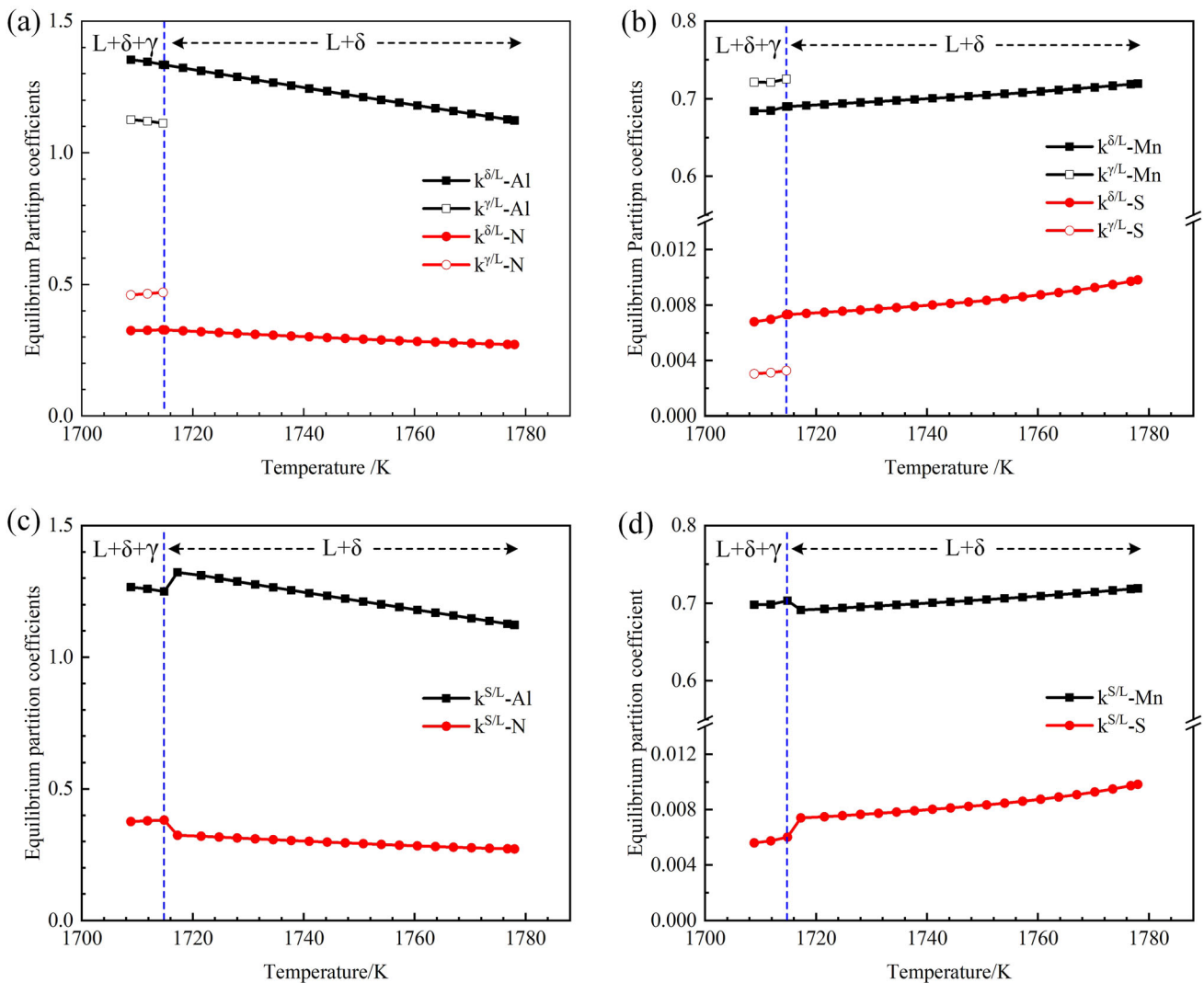


Fig. 6. The equilibrium partition coefficient of solute elements calculated by Thermo-Calc software: (a) Al and N; (b) Mn and S; (c)  $k^{S/L}$  of Al and N; (d)  $k^{S/L}$  of Mn and S.

$\delta$  and the liquid phases. However, solute S was the opposite, and it was more severe between the  $\gamma$  and the liquid phases.

In addition, when the temperature was 1715 K, a peritectic reaction took place, and the liquid,  $\delta$ , and  $\gamma$  phases coexisted simultaneously. Due to the

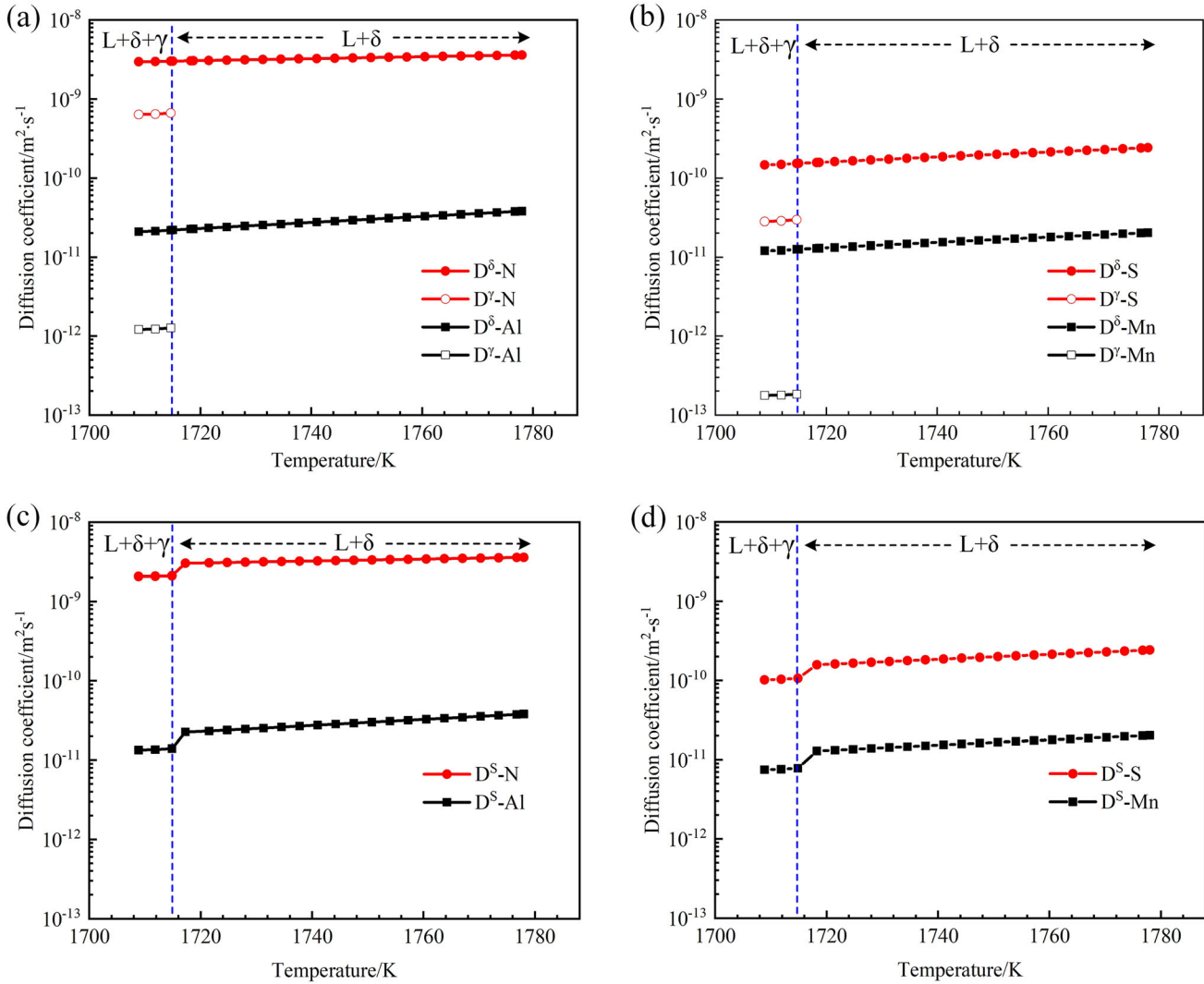


Fig. 7. The diffusion coefficients of solute elements calculated by DICTRA software: (a) Al and N; (b) Mn and S; (c)  $D^{\delta}$  of Al and N; (d)  $D^{\delta}$  of Mn and S.

partition coefficients of the solute elements in the  $\delta/L$  and  $\gamma/L$  phases being quite different, it was important to accurately calculate the partition coefficients of elements in the three-phase ( $L + \delta + \gamma$ ) coexistence zone. In this study,  $k^{S/L}$  was calculated by Eqs. 20 and 21 according to previous studies:<sup>35–38</sup>

$$k^{S/L} = m_{\delta} \cdot k^{\delta/L} + m_{\gamma} \cdot k^{\gamma/L} \quad (20)$$

$$m_{\delta} + m_{\gamma} = 1 \quad (21)$$

where  $k^{\delta/L}$ ,  $k^{\gamma/L}$ , and  $k^{S/L}$  are partition coefficients of solute elements in the  $\delta/L$ ,  $\gamma/L$ , and  $(\delta + \gamma)/L$  interfaces, respectively, and  $m_{\delta}$  and  $m_{\gamma}$  are the mass fractions of the  $\delta$  and  $\gamma$  phases in the solid phase, respectively. Then, the variable partition coefficients ( $k^{S/L}$ ) of Al, N, Mn, and S under different temperatures are shown in Fig. 6c and d. The values of  $k^{S/L}$  of these solute elements are between

$k^{\delta/L}$  and  $k^{\gamma/L}$  in the  $L + \delta + \gamma$  phase coexisting zone. The maximum partition coefficient of Mn was approximately 4.0% larger than the minimum partition coefficient during the solidification process. It was approximately 7.4% for Al, while it was approximately 40.6% and 75.5% for N and S, respectively. Obviously, the variations in the maximum and minimum partition coefficients for N and S were relatively large. Therefore, it is necessary to consider the variable partition coefficient of solute elements under different temperatures to describe the segregation behavior during the solidification process.

Figure 7a and b shows the diffusion coefficients of Al, N, Mn, and S in the  $\delta$  and  $\gamma$  phases ( $D^{\delta}$  and  $D^{\gamma}$ ) calculated by DICTRA software. The diffusion coefficients of the substitutional elements Al and Mn are far less than those of the interstitial elements N and S, and the diffusion coefficients of N are greater than those of S. The diffusion coefficients of Al, N,



Mn, and S in the  $\delta$  phase are larger than those in the  $\gamma$  phase. In addition, the difference in the diffusion coefficients of Al and Mn in the  $\delta$  and  $\gamma$  phases was larger than that of N and S. In the  $\delta$  and  $\gamma$  phases, the interstitial elements (N and S) have large diffusion coefficients, which more easily pass the layer of  $\gamma$  formed on the surface of the  $\delta$  phase and evenly distribute in the  $\delta$  and  $\gamma$  phases, while the diffusion of substitutional elements (Al and Mn) is relatively slow and difficult to pass through the  $\gamma$  layer formed by the peritectic reaction.

Similarly, the diffusion coefficients ( $D^S$ ) in the three-phase (L +  $\delta$  +  $\gamma$ ) coexistence zone are calculated by Eqs. 22 and 23, according to previous studies:<sup>35–38</sup>

$$D^S = V_\delta \cdot D^\delta + V_\gamma \cdot D^\gamma \quad (22)$$

$$V_\delta + V_\gamma = 1 \quad (23)$$

where  $D^\delta$ ,  $D^\gamma$ , and  $D^S$  are diffusion coefficients in the  $\delta$ ,  $\gamma$ , and  $\delta + \gamma$  phases, respectively, and  $V_\delta$  and  $V_\gamma$  are the volume fractions of the  $\delta$  and  $\gamma$  phases in the solid phase, respectively. Accordingly, the variable diffusion coefficients of Al, N, Mn, and S under different temperatures are shown in Fig. 7c and d. The  $D^S$  values of these solute elements are between those of the  $D^\delta$  and  $D^\gamma$  in the L +  $\delta$  +  $\gamma$  phase coexisting zone. During the solidification process, the maximum diffusion coefficients of N, S, Mn, and Al were approximately 73.0%, 138.5%, 170.4%, and 183.0% larger than the minimum coefficients, respectively. Therefore, to study the segregation behavior, the variable diffusion coefficients of solute elements under different temperatures should also be taken into account during the solidification process.

The concentration product calculated by the lever-rule and Scheil models is compared in Fig. S-1 (refer to online supplementary material). As shown in supplementary Fig. S-1a, AlN can precipitate during the solidification process, and the solid fraction ( $f_s$ ) is 0.78 and 0.83, calculated by the Scheil model and the lever-rule model, respectively. The difference in model assumptions leads to different calculated  $f_s$  values of AlN precipitation during solidification. The lever-rule model assumes that the solute elements were completely diffused in the solid phase, while these elements were not diffused in the solid phase by the Scheil model. Therefore, the  $Q_{\text{AlN}}$  calculated by the lever-rule model was smaller than that calculated by the Scheil model, so the  $f_s$  of the AlN formation calculated by the lever-rule model was larger than that calculated by the Scheil model. As shown in supplementary Fig. S-1b, the  $f_s$  values of MnS are 0.94 and 0.98 by the Scheil model and lever-rule model, respectively. In fact, as mentioned above, the formation of AlN and MnS inclusions calculated by the lever-rule model and the Scheil model were not sufficiently accurate, and

the Clyne–Kurz model considering the finite non-zero diffusion of solute elements in the solid phase can realistically represent the precipitation of AlN and MnS inclusions.

Accordingly, Eqs. 10–14 and Figs. 3–7 were calculated by the Clyne–Kurz model. During the solidification process, the concentrations of Al, N, Mn and S in the residual liquid steel were calculated as shown in supplementary Fig. S-2. [% Al] decreased with increasing solid fraction ( $f_s$ ), and [% N], [% Mn], and [% S] increased with increasing  $f_s$ , which correspond to the equilibrium partition coefficients in Fig. 6c and d.

Thereafter, the relationship between the AlN and MnS formation and solid fraction in medium Mn steel are shown in supplementary Fig. S-3. As shown in supplementary Fig. S-3a, the values of  $Q_{\text{AlN}}$  indicated that the solid fraction ( $f_s$ ) of AlN is 0.81, so AlN can precipitate during the solidification process. The  $f_s$  of MnS is 0.94, as shown in supplementary Fig. S-3b. Furthermore, the precipitation temperatures of AlN and MnS are 1738 K and 1717 K, respectively. The  $f_s$  of AlN and MnS are calculated by the Clyne–Kurz model, which are larger than the lever-rule model and less than the Scheil model. In this study, the Clyne–Kurz model was chosen, considering the nonzero diffusion of solute elements in the solid phase. The variable partition coefficients and variable diffusion coefficients of Al, N, Mn, and S under different temperatures during the solidification process, as shown in Figs. 6c and d and 7c and d, were also taken into account in the Clyne–Kurz model. In addition, as shown in supplementary Fig. S-3a, it is obvious that the variation trend of  $Q_{\text{AlN}}$  (0.0025 wt.% N) was basically consistent with that of [% N] in supplementary Fig. S-2a, illustrating that the change of in [% N] had a more significant effect on  $Q_{\text{AlN}}$  (0.0025 wt.% N). Similarly, as shown in supplementary Figs. S-2b and S-3b, the variation trend of  $Q_{\text{MnS}}$  (0.0059 wt.% S) may fall under the great influence of [% S].

In addition, based on the parameters of medium Mn steel, when the Al content is 1.93 wt.%, the critical N content of AlN formation during the solidification process is calculated as 0.0013 wt.%, as shown in supplementary Fig. S-3a. In the case of MnS, as shown in supplementary Fig. S-3b, when the Mn content is 4.96 wt.%, the critical S content of MnS formation is calculated as 0.0033 wt.%. Therefore, the N and S contents were lower than 0.0013 wt.% and 0.0033 wt.%, respectively, which prevented AlN and MnS formation during the solidification process.

### Formation Mechanism of AlN-MnS Complex Inclusions

Previous studies have shown that AlN and MnS inclusions are able to form during the solidification process, and have similar lattice parameters, while

AlN and MnS can coprecipitate.<sup>39–41</sup> In this study, the present thermodynamic calculations illustrate the formation of AlN and MnS inclusions during the solidification process. The precipitation temperatures of AlN and MnS are 1738 K and 1717 K, respectively. Therefore, AlN precipitated first, and then AlN acted as a substrate for the coprecipitation of MnS.

By experimental observation, the morphology and chemical composition of the AlN-MnS complex inclusions are shown in supplementary Fig. S-4. As shown in supplementary Fig. S-4a, b, the structure of the AlN-MnS complex inclusion is a smaller AlN with the size of  $2.0 \times 1.0 \mu\text{m}$  fits the center and a MnS inclusion with the equivalent diameter of  $4.7 \mu\text{m}$  in the outer layer, which shows that the order of precipitation temperature may be that AlN precipitates first at a relatively high temperature during solidification process and then MnS precipitates with a relatively low temperature. Therefore, the formation of AlN-MnS complex inclusions may be the AlN as a nucleation site for MnS, and then MnS wrapped around it. Meanwhile, as shown in supplementary Fig. S-4c, d, it seems that the single smaller MnS with the diameter of  $1.1 \mu\text{m}$  attaches to the surface of the larger AlN inclusion with the size of  $7.9 \times 2.4 \mu\text{m}$ . Also, AlN may precipitate first and grow up for a period of time during the solidification process, and then the MnS precipitates at the later stage of solidification, finally attaching to the surface of AlN, forming the AlN-MnS complex inclusions. Accordingly, the smaller MnS may attach one side of the larger AlN. In general, the experimental observations are in relative agreement with the results of the thermodynamic calculations, and further study is needed.

## CONCLUSION

The formation mechanism of AlN-MnS complex inclusions in Fe-5Mn-2Al-0.15C medium Mn steel was analyzed by thermodynamic calculations and the Clyne-Kurz microsegregation model. The variable partition coefficients and variable diffusion coefficients of solute elements under different temperatures were considered in the Clyne-Kurz model during the solidification process. The main conclusions can be summarized as follows:

1. In the Fe-5Mn-2Al-0.15C steel (0.0025 wt.% N, 0.0059 wt.% S), AlN and MnS inclusions were unable to form in liquid steel. With an N content higher than 0.0075 wt.%, the concentration product of Al and N could exceed its solubility product at the liquidus temperature, which led to the formation of AlN in liquid steel, while the critical S content for the formation of MnS was 0.3546 wt.%.
2. The maximum partition coefficient of Mn was approximately 4.0% larger than the minimum partition coefficient during the solidification

process. They were approximately 7.4%, 40.6%, and 75.5% for Al, N, and S, respectively. It is necessary to consider the variable partition coefficients of solute elements under different temperatures to describe the segregation behavior during the solidification process. The partition coefficients of Al were higher than 1, segregating into the dendrite interior. However, the partition coefficients for elements N, Mn, and S were lower than 1, enriching in the residual liquid steel.

3. During the solidification process, the maximum diffusion coefficients of N, S, Mn, and Al were approximately 73.0%, 138.5%, 170.4%, and 183.0% larger than the minimum coefficients, respectively. Therefore, to study the segregation behavior, the variable diffusion coefficients of solute elements under different temperatures should also be taken into account during the solidification process. The diffusion coefficients for the substitutional elements Al and Mn are far less than those for the interstitial elements N and S in the solid phase.
4. By the Clyne-Kurz model, considering the variable partition coefficients and variable diffusion coefficients, the precipitation temperatures of AlN and MnS are 1738 K and 1717 K, respectively. Based on experimental observations, the formation of AlN-MnS complex inclusions during the solidification process may be the AlN acting as a nucleation site for MnS, and then MnS wrapped or attached to the surface of AlN during the solidification process.

## SUPPLEMENTARY INFORMATION

The online version contains supplementary material available at <https://doi.org/10.1007/s11837-023-05831-5>.

## ACKNOWLEDGEMENTS

This work was supported by the National Natural Science Foundation of China (Nos. 51974079, 52174310). The authors greatly appreciate their support.

## DATA AVAILABILITY

The raw and processed data required to reproduce these findings cannot be shared at this time as the data also forms part of an ongoing study.

## CONFLICT OF INTEREST

The authors declared that they have no conflicts of interest in this work.

## REFERENCES

1. J.H. Kim, S.W. Lee, K. Lee, J.-K. Kim, and D.-W. Suh, *JOM* 71, 1366 (2019).
2. G. Su, X. Gao, D. Zhang, L. Du, J. Hu, and Z. Liu, *JOM* 70, 672 (2018).
3. L. Liu, B. He, and M. Huang, *JOM* 71, 1322 (2019).
4. R. Rana, E.D. Moor, J.G. Speer, and D.K. Matlock, *JOM* 70, 706 (2018).
5. A. Rakan, L.G. Hector, C.M. Enloe, A.-F. Fadi, and W.B. Tyson, *JOM* 70, 894 (2018).
6. S. Hu, Z. Zheng, W. Yang, and H. Yang, *Steel Res. Int.* 93, 2200191 (2022).
7. Y. Li, W. Li, N. Min, H. Liu, and X. Jin, *Int. J. Plast.* 133, 102805 (2020).
8. H. Tao, H. Zhang, and M. Wang, *Ironmak. Steelmak.* 47, 351 (2020).
9. T. Kang, J. Liang, Z. Zhao, L. Zhang, and X. Hou, *Ironmak. Steelmak.* 49, 123 (2022).
10. Y. Zhang, C. Zhao, M. Sato, G. Miyamoto, and T. Furuwara, *ISIJ Int.* 61, 1641 (2021).
11. T. Zhao, S. Rong, X. Hao, Y. Wang, C. Chen, and T. Wang, *Mater. Charact.* 183, 111595 (2022).
12. S. Zheng, C. Davis, and M. Strangwood, *Mater. Charact.* 95, 94 (2014).
13. C. Lv, Y. Wang, X. Huang, L. Zhang, Q. Fu, M. Wu, and J. Zhang, *Steel Res. Int.* 90, 1900228 (2019).
14. S. Li, S. Yang, Q. Lu, H. Luo, and W. Tao, *Metall. Trans. B* 50, 1 (2019).
15. L. Fan, S. Li, Y. Zhao, L. Jia, and J. He, *Ironmak. Steelmak.* 47, 865 (2020).
16. Y.-M. Won and B.G. Thomas, *Metall. Trans. A* 32, 1755 (2001).
17. E. Scheil and Z. Metallkd, *Int. J. Mater. Res.* 34, 70 (1942).
18. T.F. Bower, H. Brody, and M.C. Flemings, *Metall. Soc. AIME* 236, 624 (1966).
19. T.W. Clyne and W. Kurz, *Metall. Trans. A* 12, 965 (1981).
20. Ohnaka, *ISIJ Int.* 26, 1045 (1986).
21. V.R. Voller, and C. Beckermann, *Metall. Trans. A* 30, 2183 (1999).
22. Z. Liu, J. Wei, and K. Cai, *ISIJ Int.* 42, 958 (2002).
23. S.K. Choudhary and A. Ghosh, *ISIJ Int.* 49, 1819 (2009).
24. Y. Liu, L. Zhang, H. Duan, Y. Zhang, Y. Luo, and A.N. Conejo, *Metall. Trans. A* 47, 3015 (2016).
25. C. Shi, X. Chen, and H. Guo, *Metall. Mater.* 19, 295 (2012).
26. H. Liu, J. Liu, S. Michelic, F. Wei, C. Zhuang, Z. Han, and S. Li, *Ironmak. Steelmak.* 43, 171 (2016).
27. M. Alba, M. Nabeel, and N. Dogan, *Steel Res. Int.* 91, 1900477 (2020).
28. M. Nabeel, M. Alba, A. Karasev, P.G. Jönsson, and N. Dogan, *Metall. Trans. B* 50, 1674 (2019).
29. M. Alba, M. Nabeel, and N. Dogan, *Ironmak. Steelmak.* 48, 379 (2021).
30. D. Liu, Z. Xue, and S. Song, *Steel Res. Int.* 93, 2200551 (2022).
31. M.-K. Paek, J.-M. Jang, M. Jiang, and J.-J. Pak, *ISIJ Int.* 53, 973 (2013).
32. H. Liu, S.K. Michelic, S. Shen, X. Su, B. Wu, and H. Ding, *Steel Res. Int.* 87, 1723 (2016).
33. W. Wang, H. Zhu, Y. Han, J. Li, and Z. Xue, *Ironmak. Steelmak.* 48, 1038 (2021).
34. T. Zhang, Y. Chen, G. Cheng, X. Yang, X. Chen, J. Pan, Y. Huang, and Q. Wang, *Steel Res. Int.* 93, 2200478 (2022).
35. P. Lu, H. Li, H. Feng, Z. Jiang, H. Zhu, Z. Liu, and T. He, *Metall. Trans. B* 52, 2210 (2021).
36. L. Gui, M. Long, Y. Huang, D. Chen, H. Chen, H. Duan, and S. Yu, *Metall. Trans. B* 49, 3280 (2018).
37. Y. Huang, M. Long, P. Liu, D. Chen, H. Chen, L. Gui, T. Liu, and S. Yu, *Metall. Trans. B* 48, 2504 (2017).
38. Y. Ueshima, S. Mizoguchi, T. Matsumiya, and H. Kajioka, *Metall. Trans. B* 17, 845 (1986).
39. L. Martin, W. Tomasz, P.-K. Erwin, Z. Sabine, and K. Ernst, *Steel Res. Int.* 89, 1700342 (2018).
40. J.H. Park, D.-J. Kim, and D.J. Min, *Metall. Trans. A* 43, 2316 (2012).
41. Y. Chen, Y. Wang, and A. Zhao, *J. Iron Steel Res. Int.* 19, 51 (2012).

**Publisher's Note** Springer Nature remains neutral with regard to jurisdictional claims in published maps and institutional affiliations.

Springer Nature or its licensor (e.g. a society or other partner) holds exclusive rights to this article under a publishing agreement with the author(s) or other rightsholder(s); author self-archiving of the accepted manuscript version of this article is solely governed by the terms of such publishing agreement and applicable law.